Ore Geology Reviews 171 (2024) 106176

Contents lists available at ScienceDirect

Ore Geology Reviews

journal homepage: www.elsevier.com/locate/oregeorev

Characterization of Co-bearing pyrite from the SEDEX Tuolugou Co(Au) deposit, northern Qinghai-Tibet Plateau, China

Sida Niu [a,b], Huaying Wu [a,b,*], Xianglong Niu [a,b], Yingchao Wang [a,b], Jan Marten Huizenga [c,d,e], Jiahao Chen [a,b], Guangyao Liu [f], Lingchao Mo [a,b], Zhiguang Chen [g], Wenjun Li [h]

[a] Institute of Mineral Resources Research, China Metallurgical Geology Bureau, Beijing 101300, China
[b] Mineral Comprehensive Utilization Research and Development Center, China Metallurgical Geology Bureau, Beijing 101300, China
[c] Faculty of Environmental Sciences and Natural Resource Management, Norwegian University of Life Sciences, P.O. Box 5003, NO-1432 Ås, Norway
[d] Economic Geology Research Institute (EGRU), College of Science and Engineering, James Cook University, Townsville, Queensland 4811, Australia
[e] Department of Geology, University of Johannesburg, PO 524, Auckland Park 2006, South Africa
[f] State Key Laboratory of Geological Processes and Mineral Resources, Institute of Earth Sciences, China University of Geosciences, Beijing 100083, China
[g] PT. Wanxiang Nickel Indonesia, Centennial Tower Lantai 35 Unit A&B Jl, Gatot Subroto No. Kav. 24-25, Karet Semanggi, Kecamatan Setiabudi, Kota Jakarta Selatan 12930, Indonesia
[h] Key Laboratory of Mineral Resources, Institute of Geology and Geophysics, Chinese Academy of Sciences, Beijing 100029, China

ARTICLE INFO

Keywords:
Cobalt
East Kunlun
Isomorphism
Pyrite
SEDEX deposit

ABSTRACT

The Tuolugou sedimentary-exhalative (SEDEX) Co-Au deposit is located in the eastern Kunlun metallogenic belt of the northern Qinghai-Tibet Plateau in China. Pyrite is the prevalent Co-hosting sulfide mineral that occurs in the Tuolugou deposit. In this study, we investigated mineral characteristics of Co-bearing pyrite and effect of Co on crystal structure of the pyrite to obtain a better understanding of Co mineralization. Three pyrite generations were identified, including Co-barren pyrite (Py-1, formed during the early mineralization stage I, with Co content of 1-3844 ppm), Co-rich pyrite (Py-2, formed during the sedimentary-exhalative stage II, Co content 15–36522 ppm), and Co-rich pyrite (Py-3, formed during metamorphic stage III, with Co contents of 448–10505 ppm in Py-3A, and 1371–14904 ppm in Py-3B). As Co enters the pyrite structure, it is discovered that the octahedrons in pyrite is twisted and tilted, the lattice parameters (a_0) rise, and the sulfur atom positions alter. The Co-rich Py-2 shows a similar REE and trace element distribution as those in quartz albitite, which indicates that Co mineralization is related to SEDEX genesis. Subsequent metamorphism resulted in additional Co enrichment. This detailed study of Co-bearing pyrite provides insights on the details of isomorphism Co in pyrite similar to the situation of this deposit as medium–low Co grade.

1. Introduction

Cobalt is derived from sediment-hosted hydrothermal deposits (60 %), magmatic sulfide deposits (as a byproduct of Ni mining) (23 %), laterite deposits (15 %), and hydrothermal vein-type deposits (2 %) (Slack et al., 2017; Vasyukova and Williams-Jones, 2022). Except for a small number of independent deposits, Co is mainly produced as an associated metal (Su et al., 2023).

The discovery of Co resources in the eastern Kunlun metallogenic belt indicates its potential for Co exploitation in this region (Li et al., 2001; He et al., 2022). With the exception of magmatic polymetallic sulfide deposits, Co is barely exploited in the eastern Kunlun metallogenic belt. The Late Ordovician to Early Silurian formation age and sedimentary exhalative (SEDEX) nature are proposed by Feng et al. (2009, 2011).

Pyrite is a significant Co-bearing ore mineral that forms through a variety of processes (Hazen et al., 2017; Hazen and Morrison, 2022; Lu, 2022). The primary host mineral for Co in the Tuolugou deposit is pyrite (Feng et al., 2011). The mineralogical properties of pyrite, including its crystal structure, chemical composition, and thermo-electricity, have been studied by numerous researchers (Abraitis et al., 2004; Cook et al., 2009; Niu et al., 2016; Zhu et al., 2018; Yuan et al., 2018; Xian et al., 2018; 2019; Zhang et al., 2021; 2022; Sun et al., 2024). Pyrite could have elevated Co consents through a variety of processes of magmatism, sedimentary and metamorphism (Qiu et al., 2021). However, detailed mineralogical studies of Co-bearing pyrite at submicron to nano scales

* Corresponding author at: Institute of Mineral Resources Research, China Metallurgical Geology Bureau, Beijing 101300, China.
E-mail address: wuhuaying@cmgb.cn (H. Wu).

https://doi.org/10.1016/j.oregeorev.2024.106176
Received 17 December 2023; Received in revised form 16 July 2024; Accepted 20 July 2024
Available online 22 July 2024

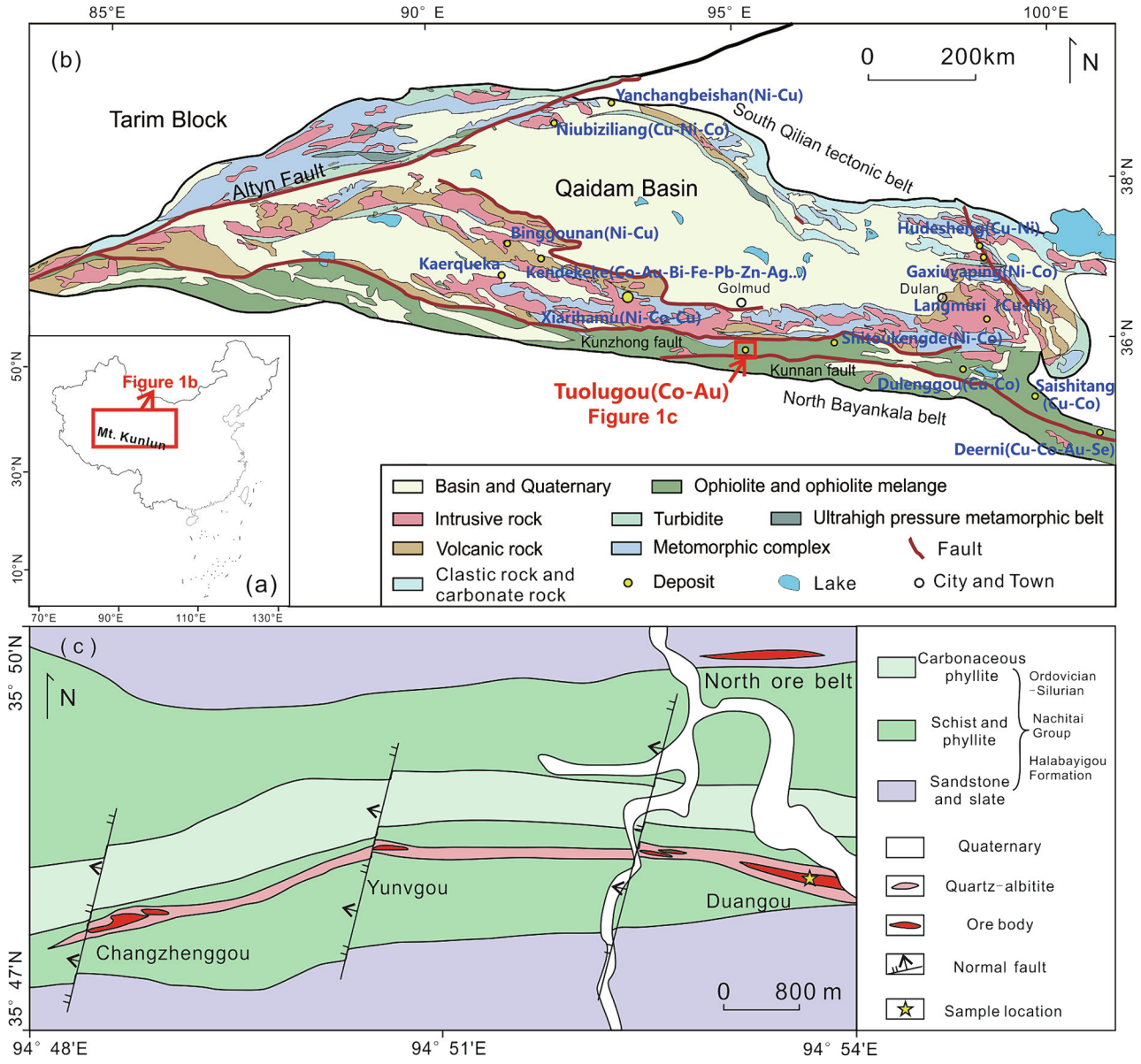

Fig. 1. Location (a), regional geological setting of East Kunlun-Northern Qaidam region (b) and detailed geological map of the Tuolugou deposit (c) (modified after Feng et al., 2009).

are mostly unknown in the Tuolugou deposit.

We used a variety of different methods to characterize the pyrite in the Tuolugou deposit (Qinghai Province, China), including electron probe microanalysis (EPMA), (laser-ablation) inductively coupled plasma mass spectrometry (ICP-MS), transmission electron microscopy (TEM), high-resolution transmission electron microscopy (HRTEM), high-angle annular dark-field scanning transmission electron microscopy (HAADF-STEM) element mapping, and powder X-ray diffraction (XRD). This paper describes the elaborate Co-mineralization process of the Tuolugou deposit and assigns its origin systematically. We concentrated in a detailed major-trace geochemistry analysis and nanoscale textural study of the Co-bearing pyrite from the study area.

2. Geological background and pyrite types

The Tuolugou deposit is situated in the eastern Kunlun orogenic belt in the Qinghai Province. The eastern Kunlun orogenic belt is located in the northeastern margin of the Qinghai-Tibet plateau (northwest China) and forms the western part of the Central Orogenic Belt (Fig. 1a). It experienced a long and complex geodynamic evolution, including the formation of an ancient continent nucleus, the formation of oceanic basalt plateau, Early Mesozoic orogenic processes, and subsequent intracontinental tectono-thermal events (Xu et al., 2001; Song et al., 2018; Dong et al., 2018; Yu et al., 2020). The Caledonian Qilian southern-margin subduction complex zone, also known as the suture zone, was formed 490 ~ 500 million years ago and marks the boundary between the Qilian terrane and the North Kunlun-Qaidam terrane. Numerous Variscan granitoids with ages of 207–227 Ma and Indosinian granitoids with ages of 257–376 Ma intruded the northern Kunlun belt and form a nearly EW-trending magmatic belt (Feng et al., 2009; Wang et al., 2022). Intensive tectonic-magmatic activities resulted in polymetallic Cu-Ni-Co-Au-Fe mineralization in the eastern Kunlun orogenic belt (i.e., the eastern Kunlun metallogenic belt). In addition to the Tuolugou deposit, there are more than ten giant to medium sized Cu-Ni-Co-Au-Fe ore deposits and mineralized spots present, including the Xiarihamu, Zhongyou, Kendekeke, Galinge, Niukutou, Yemaquan, Shitoukengde, Langmuri, Dulenggou, Haisi, Xiaowolong, Shengli, and Deerni deposits.

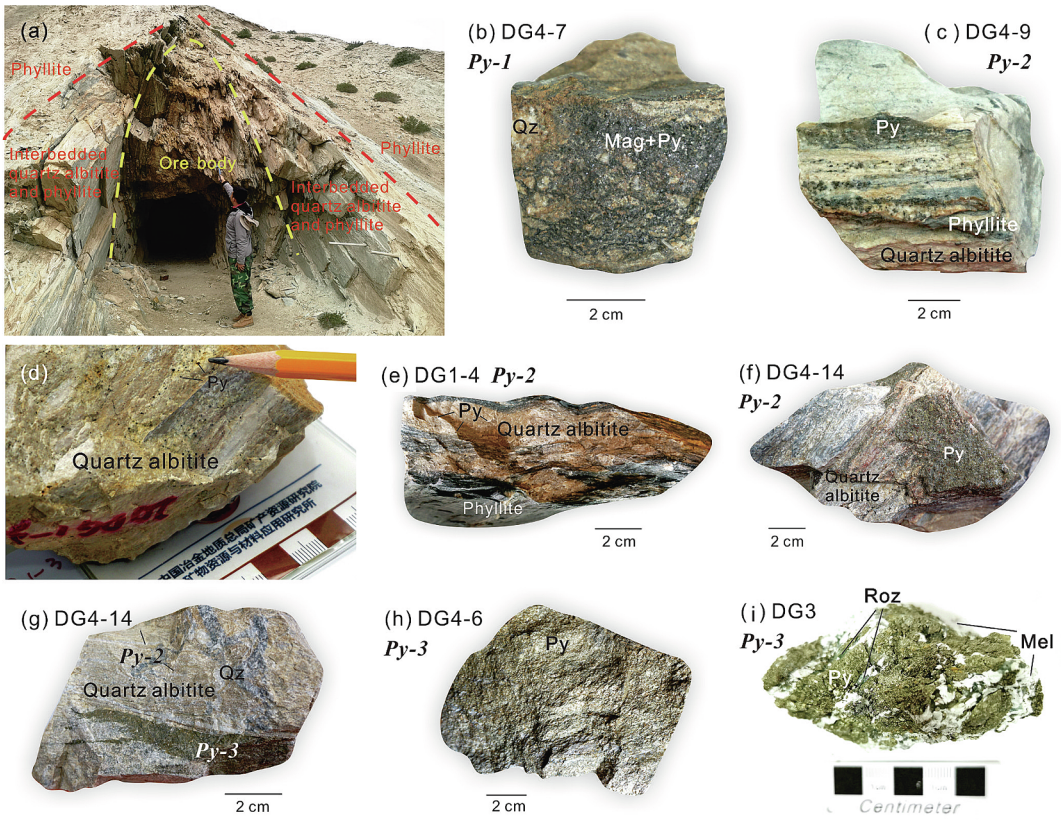

Fig. 2. Outcrop and representative hand specimens comprising pyrite from the Tuolugou deposit. (**a**) Outcrop of quartz albitite and ore body. (**b**) Pyrite-magnetite stockwork. (**c**) Laminated and (**d**) disseminated pyrite in quartz albitite. (**e**) Phyllite intercalated with pyrite-bearing quartz albitite with disseminated pyrite. (**f**) Patched pyrite and (**g**) vein structure in quartz albitite. (**h, i**) Massive structure. Py = pyrite, Mag = magnetite, Roz = rozenite, Mel = melanterite.

Table 1
Occurrence, structure, lattice parameters and cobalt content of the pyrite samples from the Duangou ore section, the Tuolugou deposit.

	Occurrence	Ore texture, structure and mineral assemblage	Pyrite type	Cobalt content in pyrite (ppm)	Lattice parameter (Å) and Chi2	Z(Å^3)
DG4-7	Pyrite + magnetite	Euhedral-subhedral (Py-1) + quartz + magnetite Stockwork	Py-1	355	5.41647(2) Chi2 = 2.55	158.909 (1)
DG3	In center of the oxidated ore body (detailed description in Niu et al., 2023)	Anhedral Py-3 Densely Disseminated	Py-3	837	5.41773(2) Chi2 = 2.25	159.020 (1)
DG1-4	Pyrite-bearing quartz albitite interlayered with phyllite	Anhedral and euhedral-subhedral (Py-2) + quartz + albite Disseminated and scattered	Py-2	946	5.41734(2) Chi2 = 2.31	158.986 (1)
DG4-6	In the central ore body	Anhedral Py-3 Massive	Py-3	3063	5.41809(3) Chi2 = 2.85	159.052 (1)
DG4-14	In quartz albitite	Anhedral and euhedral-subhedral (Py-2) + quartz + albite Agglomerated-vein	Py-2	3228	5.41784(3) Chi2 = 2.31	159.030 (1)
DG4-9	In quartz albitite	Anhedral and euhedral-subhedral (Py-2) + quartz + albite Laminated	Py-2	10,248	5.42024(4) Chi2 = 2.12	159.241 (2)

The Tuolugou Co-Au deposit is characterized by an east–west striking mineralized zone in between the Kunzhong and Kunnan faults (Fig. 1b). It has estimated Co resources of > 16,000 t with an average Co grade of 0.06 % and a maximum Co grade of 0.46 % (Feng et al., 2011). The deposit is hosted within the limb of the east–west striking Jiuqigou anticline in low-grade metamorphic volcano-sedimentary rocks (Feng et al., 2009). The volcano-sedimentary rocks are rich in Co, Au, and other metals during Caledonian crustal extension. The lenticular and stratiform orebodies occur in quartz-sericite schists and quartz albitites (Fig. 1c) and are interlayered with phyllites (Fig. 2a).

The metavolcanic-sedimentary rock segment in the Tuolugou deposit develops a typical lamellar hydrothermal exhalation sedimentary quartz albitite (Fig. 2; Feng et al., 2009; 2011). Generally, quartz albite indicates a SEDEX genesis (Ma et al., 2004; Luo et al., 2017). In the Tuolugou deposit, quartz albitite is produced in layered or quasi-layered form and forms rhythmic laminae with sericite quartz schist and chlorite sericite quartz schist, and occurs within 30 m on both sides of the ore body (Fig. 2a, c, e, f). Mineralization in the Tuolugou deposit is

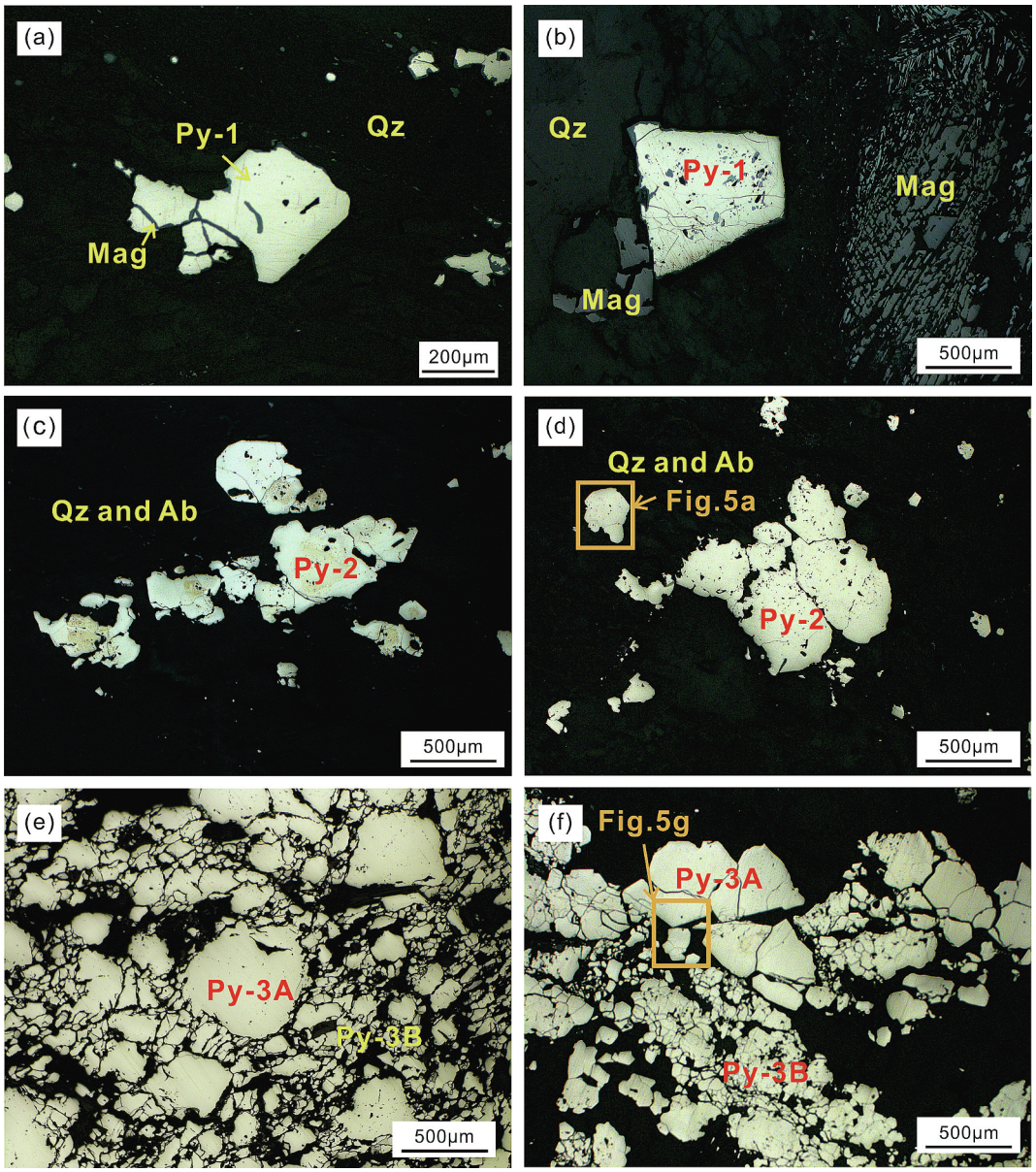

Fig. 3. Photomicrographs of pyrite from the Tuolugou deposit. (a, b) Idiomorphic to hypautomorphic Py-1 and magnetite. (c) Hypautomorphic to xenomorphic Py-2. The inset refers to Fig. 5a. (d) Idiomorphic Py-2 hosted in quartz albitite. (e, f) Xenomorphic coarse-grained Py-3A and finer grained Py-3B. The inset in (f) refers to Fig. 5g. Ab = albite, Py = pyrite, Mag = magnetite, Qz = quartz.

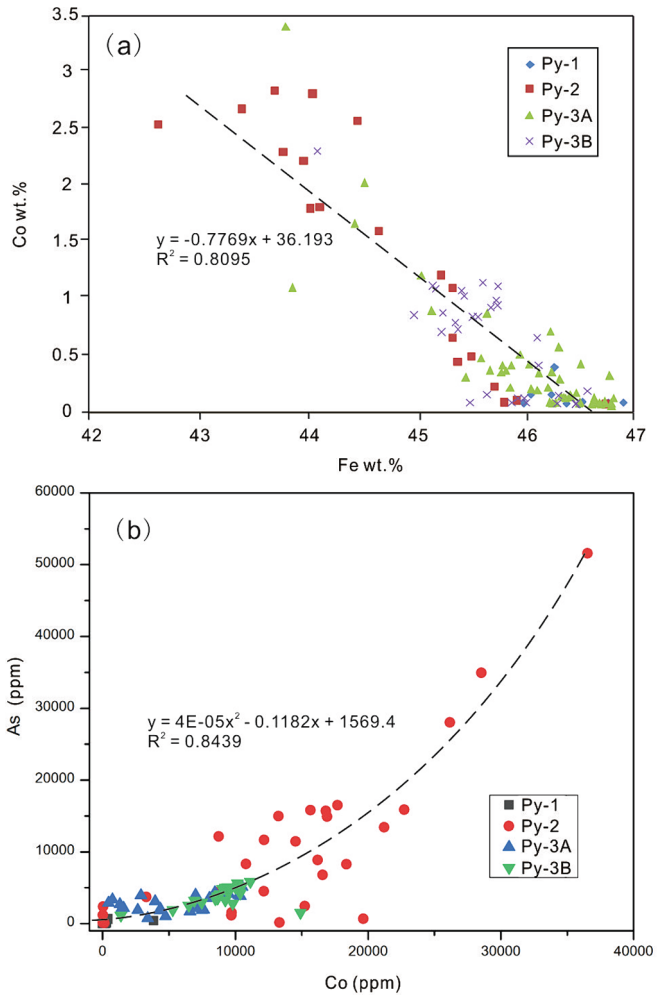

Fig. 4. Plots of (**a**) Fe-Co (EPMA) and (**b**) Co-As (LA-ICP-MS) of pyrite from the Tuolugou deposit.

dominantly characterized by pyrite and minor arsenopyrite, chalcopyrite, bornite, sphalerite, and native gold, and trace amounts of hengleinite. Gangue minerals include quartz, albite, carbonate, sericite, and chlorite.

Pyrite samples were collected from the Duangou ore section of the Tuolugou deposit (location shown in Fig. 1c, detailed information displayed in Table 1). The pyrite displays faint yellow color, indicating brassy yellow when exposed to weathering. The occurrence, mineral assemblages and crosscutting relationships indicate that the Co mineralization appeared in three episodes, further subdivided into four substages (Figs. 2 and 3).

The early mineralization stage (stage I) produced Py-1, quartz and magnetite. It is related to stockwork and disseminated mineralization (Fig. 2b). Py-1 occurs as euhedral-subhedral cubic crystals associated with quartz and fine-grained magnetite. Interstitial and inclusive structures can both be observed (Fig. 3a, b).

The *syn*-sedimentary and fluid pulsing stage (stage II) is characterized by mineral assemblages of Py-2, quartz, and albite. Py-2 occurs as fine-grained anhedral (Fig. 3c) and euhedral-subhedral pyritohedron crystals (Fig. 3d) within quartz albitites (Fig. 2c-g). Py-2 occurs as laminated (Fig. 2c), disseminated (Fig. 2d and e), patched (Fig. 2f), and vein-type ores (Fig. 2g).

The superimposed-metamorphism stage (stage III) Py-3 veins cross cut the stage II Py-2. Py-3 is anhedral and massive (Fig. 2h, i) and can be subdivided into a coarse-grained (>300 μm, sub type Py-3A) and a fine-grained, fragmented pyrite (<300 μm, subtype Py-3B) (Fig. 3e, f).

3. Analytical methods

3.1. Pyrite major and trace element geochemistry

Major element compositions of the pyrite in this study were determined at the Chinese Academy of Geological Sciences using a JXA-iHP200F Hyper Probe electron microprobe. Wavelength dispersive spot analyses were done using a 20 kV accelerating voltage and a beam current of 20nA, and a beam diameter of 5 μm. Details of EPMA methods are described in Yang et al. (2022). Standard substances refer to GB/T 15074-2008 general rules for EPMA analysis. Element mapping was done using a 20 kV accelerating voltage, a beam current of 50nA, and a beam diameter of 1 μm. Data were corrected on-line using a modified ZAF correction.

3.1.1. Trace element geochemistry of pyrite and quartz albitite

Trace element geochemical analyses of pyrite powder (<200 mesh) were done at Shandong Bureau of China Metallurgical Geological Bureau. Trace elements analyses were performed by a Thermo Scientific XSeries 2 ICP-MS (YQ006) with the GB/T 14506.30-2010 standard. Trace elements including REEs of quartz albitite were analyzed at the Northwest University, China, using an Agilent 7500a plasma mass spectrometer.

3.1.2. In-situ trace element analysis of pyrite

In-situ trace elements analyses of the pyrite were performed on a 193 nm Coherent GeoLas Pro ArF Excimer laser coupled to an Element XR SF-ICP-MS instrument at the Metallogenetic Elements and Isotopes Laboratory (Institute of Geology and Geophysics, Chinese Academy of Sciences). Ablation was performed using a 60 μm diameter ablating spots at 5 Hz with an energy of 5 J/cm^2 for 60 s after measuring the gas blank for 30 s. A pre-ablation of three laser pulses was done prior to each analysis, and a 30 s washout between the analyses. The carrier (He) and make-up gas (Ar_2) flows were optimized by a spot ablation of the NIST SRM 612 to obtain maximum signal intensities, while keeping ThO/Th mass ratio < 0.5 ‰ and the U/Th mass ratio at 0.95–1.05. Trace element concentrations were calibrated against the ARM-2 with ^{57}Fe as the internal standard element and using USGS BCR-2G and BIR-1G glass as a quality monitor (Wu et al. 2019; Xue et al., 2023; Li et al., 2023). Data reduction was done using the GLITTER software.

3.2. TEM, HRTEM and HAADF-STEM of pyrite

Pyrite mineral powder (<200 mesh) was prepared for ultra-thin sections for TEM and HRTEM analyses. The samples were prepared by depositing several droplets of a nanoparticle-ethanol mixture onto a carbon coated Cu-grid, and then treated with ion thinning. TEM and HRTEM analyses were done at the Beijing General Research Institute of Mining & Metallurgy Technology Group using a JEOL JEM2100 high-resolution transmission electron microscope with an accelerating voltage of 200 kV, a beam current of 105–106nA, and a beam spot size of 1 μm. HAADF-STEM element mapping was done using a Thermo Fisher Scientific Talos F200X instrument at China University of Geosciences (Wuhan, China) with an accelerating voltage of 200 kV, current of 0.413nA, and spot size of 6 μm (STEM mode).

3.3. Pyrite XRD

Powder XRD analysis of the pyrite crystals (<200 mesh) was carried out at room temperature at the China University of Geosciences Beijing using a Rigaku SmartLab diffractometer with Cu K-alpha radiation (40 kV, 200 mA) and a graphite monochromator. A step scan mode was employed with a 2θ step width of 0.02° and a sampling time of 1 s in the range of 20° to 155°. The Rietveld profile matching method was used to refine the unit cell parameters using Fullprof WinPLOTR software (JBT = 2, profile matching was calculated with a constant scale factor).

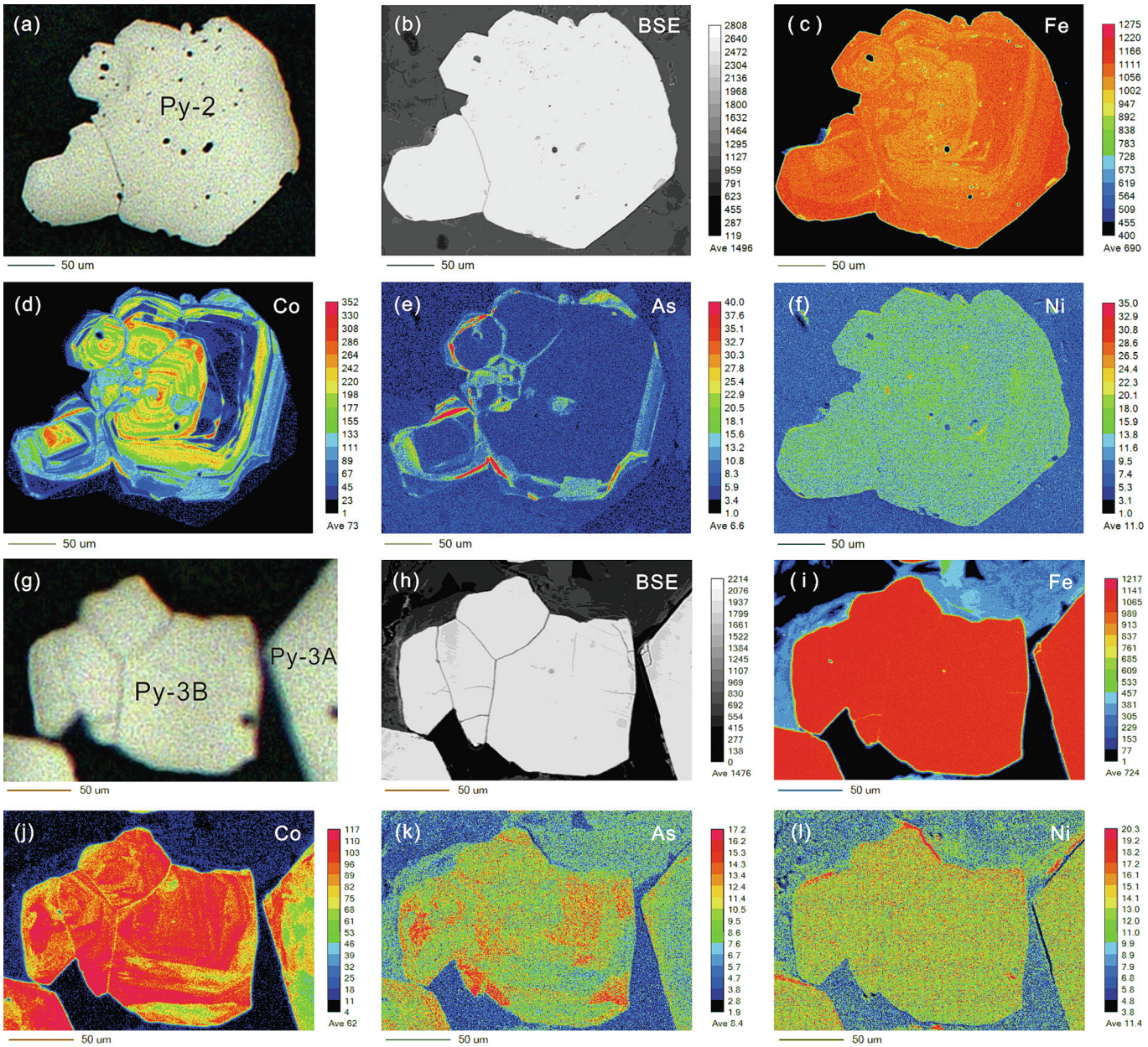

Fig. 5. Photomicrographs (**a**, **g**), backscattered electron images (**b**, **h**), and pyrite element scanning maps for Fe (**c**, **i**), Co (**d**, **j**), As (e, k), and Ni (**f**, **l**) from the Tuolugou deposit.

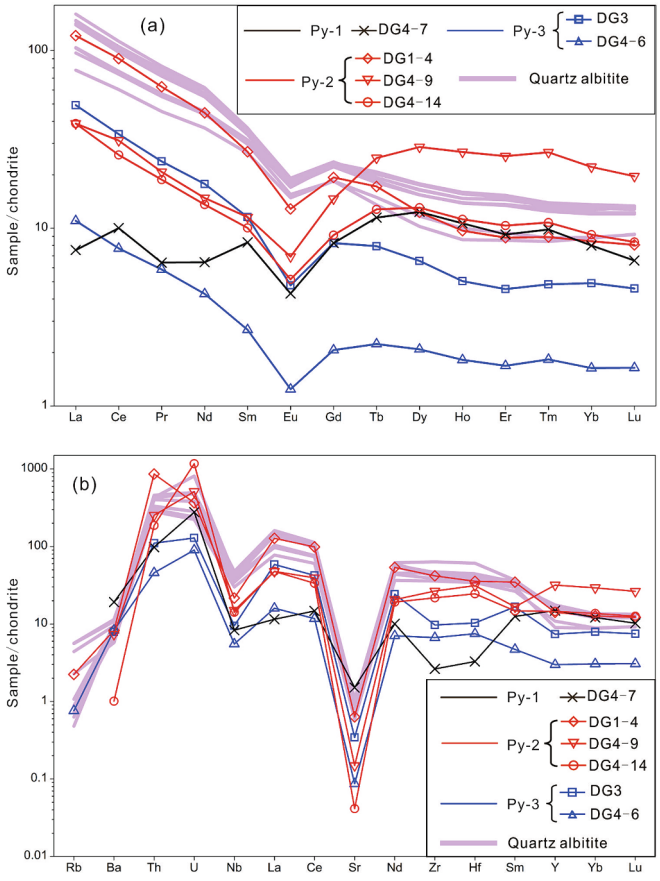

Fig. 6. Chondrite-normalized (a) REE patterns and (b) trace element spider diagrams for pyrite and quartz albitite from the Tuolugou deposit. Chondrite values are from Sun and McDonough (1989).

The Rietveld refinement method was used to get the atomic coordinates of pyrite (JBT = 0) (Rietveld, 1967; Rodríguez-Carvajal, 1993).

4. Results

4.1. Pyrite geochemistry

Supplementary Table 1 lists the pyrite EPMA results. The Co and Fe contents of the three pyrite types are shown in Fig. 4a and As-Co plots are presented in Fig. 4b. The Fe and Co show a negative correlation, while S is relatively constant (51.4–53.7 wt%) with an average value of 53.0 wt%. Py-1 shows a minor variation of the Fe content (46.0–46.9 wt %), with an average value of 46.4 wt%. The Fe content of Py-2 has a larger variation (42.6–46.8 wt%, with an average value of 44.7 wt%). The Fe content of Py-3A varies between 43.8–46.8 wt% (average value of 46.1 wt%). The Fe content of Py-3B ranges from 44.1 to 46.6 wt%, with an average value of 45.7 wt%. Backscattered electron images and pyrite element maps for the major elements – Fe, Co, As, and Ni are shown in Fig. 5.

Pyrite chondrite-normalized REE patterns (Fig. 6a, data shown in Supplementary Table 2) show LREE enrichment relative to the HREE with LREE/HREE ratios of 1.5–7.8. The pyrite is characterized by an Eu negative anomaly (Eu/Eu* = 0.54–0.61). The different pyrite types show contrasting geochemical characteristics, in particular with regards to the degree of enrichment of Th, U, Zr, and Hf (Fig. 6b). Py-2 shows enrichment of Th, U, Zr, and Hf. Py-1 shows strong depletion of Zr and Hf, whereas Py-3 shows a weak Zr and Hf depletion.

The in-situ trace element geochemistry of pyrite is shown in Supplementary Table 3 and Figs. 4 and 7–8. Co content is 1–3844 ppm (average of 558 ppm) in Py-1, 15–36522 ppm (average value of 13778 ppm) in Py-2, 448–10505 ppm (average value of 5571 ppm) in Py-3A, and 1371–14904 ppm (average value of 8909 ppm) in Py-3B. Ni and As contents in Py-1 are in the range of 31–2392 ppm and 3–693 ppm, respectively. Ni content in Py-2 ranges from 29 to 5648 ppm and As content ranges from 100 to 51574 ppm. Py-3A shows Ni content ranging from 67 to 1657 ppm and As content ranging from 773 to 5121 ppm. Py-3B has Ni and As contents of 384–2108 ppm, 1137–5860 ppm, respectively.

4.2. Quartz albitite geochemistry

Supplementary Table 4 displays the quartz albitite's trace element geochemistry data. Chondrite-normalized REE patterns for the quartz albitite show LREE enrichment relative to HREE with LREE/HREE ratios of 2.41–3.76 and Eu negative anomalies (Eu/Eu*=0.61–0.66) (Fig. 6a). The quartz albitite is characterized by Nb and Sr depletion, and Th and U enrichment (Fig. 6b).

4.3. Nanoscale structure of Co-bearing pyrite

Py-2 with the highest Co content was selected as the representative sample for TEM, HRTEM and HAADF-STEM analyses. The samples are extremely fragile under the electron beam as they can flinch within a few minutes during electron bombardment. The pyrite crystal planes are continuous and consistent according to the detailed nanoscale structure in TEM and HRTEM images (Fig. 9). Lattice distortion such as stacking faults can occasionally be observed (Fig. 9b-c). The d values of the (1 0 0) lattice planes are calculated to be 0.273 nm (d_1), 0.275 nm (d_2), and 0.253 nm (d_3) (Fig. 9d). The d_4 value of the (4 1 0) lattice plane is calculated to be 0.132 nm (Fig. 9e, f). No clear grain boundaries related to mineral inclusions are observed in the pyrite. Under HAADF-STEM, the sample tends to shrink (Fig. 10a). The S atoms occur in elliptical clusters, in which S occurs as a relatively high-value center with a diameter of 10–40 nm (Fig. 10b). Fe, Co, Ni and As show homogeneous distribution (Fig. 10c-f).

With increasing Co content in pyrite, the cell parameters (a_0) increase, and there is a change of the atom coordinates of sulfur, bond length, and bond angle (Table 1, Figs. 11 and 12). For sample DG4-7, with a Co content of 355 ppm, coordinate of sulfur atom is a = b = c = 0.38690 (3) Å and for sample DG4-9, with a Co content of 10248 ppm, coordinate of sulfur atom is a = b = c = 0.38599(2) Å (see Table 2 and Fig. 13 for details).

5. Discussion

5.1. Co enrichment in pyrite

Co and Ni are common elements which enter the crystal lattice of pyrite to substitute Fe (Abraitis et al., 2004). There is potential for Co and Ni exploration in the eastern Kunlun metallogenic belt. The octahedral site preference energy (OSPE) of Co^{2+} is smaller than that of Ni^{2+} (Burn, 1993; Niu et al., 2016). The larger the OSPE value of the ion, the stronger its tendency to preferentially occur in an octahedral lattice site. During mineral crystallization, transition metal ions with larger OSPE preferentially enter the mineral crystal structure. Ni prefers to mineralize during the magmatic period and Co might mineralize during late-stage magmatism and hydrothermal stage (Lu et al., 2017). Thus, quite a few magmatic deposits in the eastern Kunlun metallogenic belt are with Ni mineralization (He et al., 2022), in contrast to the Co-rich Tuolugou deposit with SEDEX genesis.

Element contents between three pyrite generations have distinct characteristics. Py-1 has similar Ni, As, Co, and Mg contents in the Tuolugou deposit (Fig. 8). Whereas, the Co and As contents are higher than Ni and Mg in Py-2 and Py-3. The Co is the highest in Py-2, followed by Py-3B and Py-3A, and Py-1, which has the lowest Co content. The

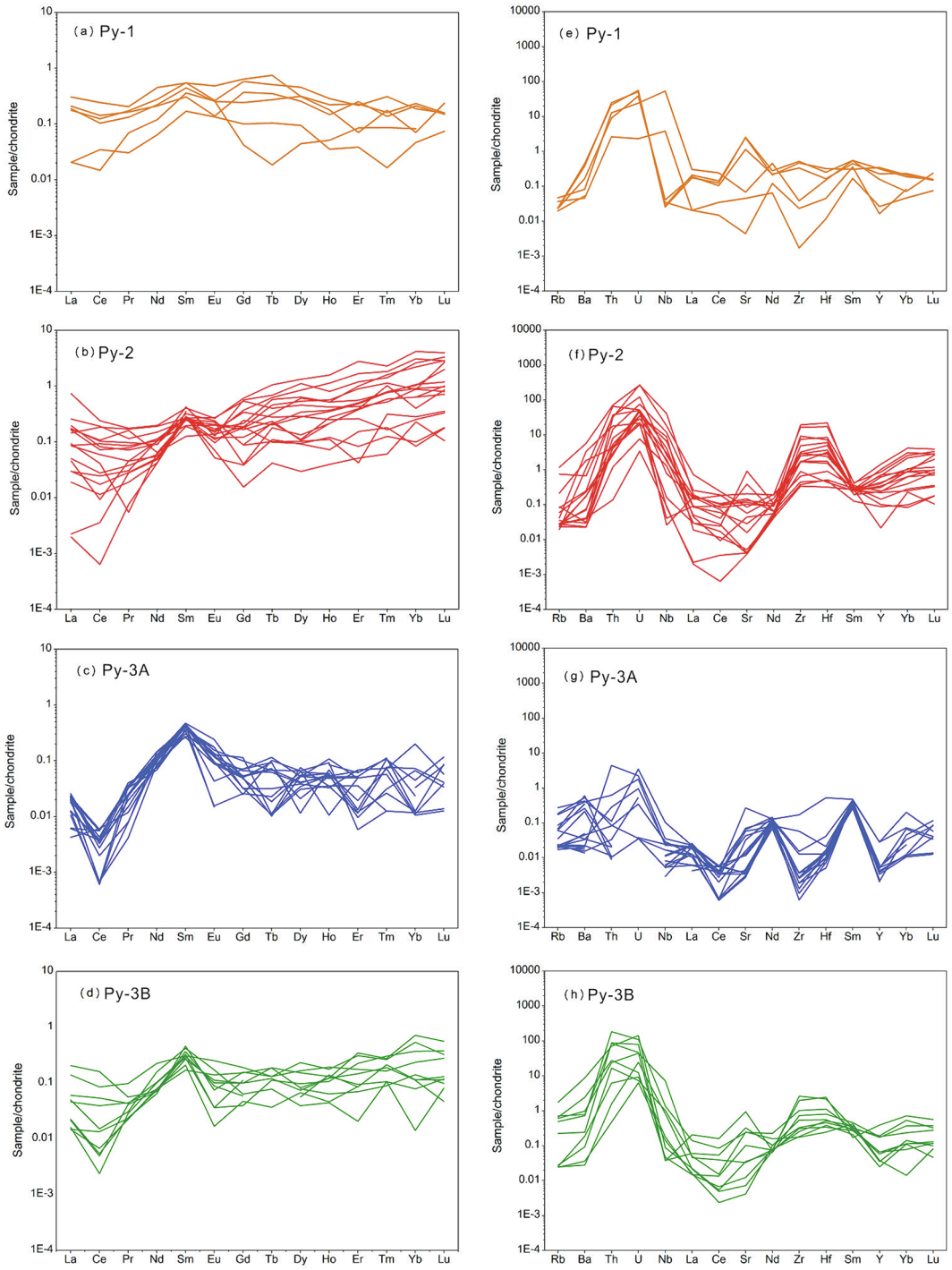

Fig. 7. In-situ (a) chondrite-normalized REE patterns and (b) trace element spider diagrams for pyrite from the Tuolugou deposit. Chondrite values are from Sun and McDonough (1989).

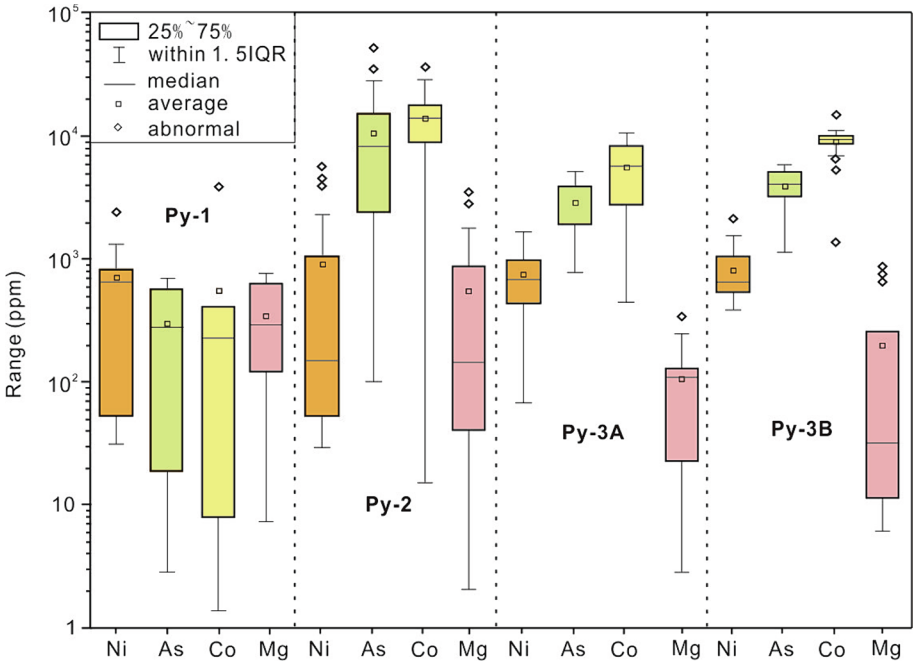

Fig. 8. (**a**) Ni-As-Co box plots and (**b**) Co-Ni plots of pyrite from the Tuolugou deposit.

enrichment of the high field-strength elements (HFSE) U, Th, Zr and Hf in Py-2 indicates the function of the hydrothermal activities (Fig. 6b, Huang et al., 2011; Niu, 2012). In Py-1 and Py-3, Zr and Hf are depleted, indicating that these pyrite types went through the neap of the SEDEX mineralization, or the very beginning (Py-1) and ending (Py-3) of the sedimentary-exhalative process.

The characteristics of the three pyrite types can be important clues to identify the three-stage mineralization processes. The early mineralization stage I (Co-barren) contains Py-1 with minor amounts of Co (Fig. 14a). The sedimentary-exhalative stage II contains Co-rich Py-2 that is closely related with quartz albitite. Euhedral Py-2 has a concentric structure (Fig. 5a-f), indicating that it formed as a result of oscillating hydrothermal fluid pulsations. The increase of As in the Py-2 outer zone indicates low-temperature, late-stage Py-2 mineralization (Zhang et al., 2021), indicating late cooling by seawater (Fig. 14b).

Early Py-1 and late Py-3 are cubic whereas Py-2 has a pentagonal dodecahedron structure (Yuan et al., 2018; Alam et al., 2019), indicating Co enrichment. Py-3, which was formed during the metamorphic stage III, displays a lower Co content than Py-2 (Py-3A coarse grain; Py-3B fine grain with micro fractures; Fig. 14c). Regional metamorphism resulted in slight enrichment of Co from Py-3A to Py3B (Fig. 5g-l and 14c; Su et al., 2019; Witt et al., 2020).

5.2. *Effect of Co on the pyrite crystal structure*

The Co and Fe contents in the pyrite of the Tuolugou deposit display a negative correlation (Fig. 4a) indicating isomorphism. Co-Fe substitution might promote the As-S substitution (Fig. 4b). No grain boundaries were observed in the pyrite (Fig. 9), which implies that Co-rich mineral inclusions such as cattierite (CoS_2) or linnaeite (Co_3S_4) are absent. Therefore, it can be concluded that Co occurs in pyrite as a result of isomorphic replacement of Fe, which is confirmed by the homogeneous distribution of Fe, Co, Ni, and As in pyrite (Fig. 10c-f). Sulfur displays as a cluster (Fig. 10b), which might be related to the sample vulnerability under the high-power electron beam convergence.

The mineral phases present in sample DG4-7 are pyrite, and minor rozenite, goethite, and hematite (Fig. 12a). The mineral phases present in sample DG4-9 are pyrite and rozenite (Fig. 12b). Pyrite is an equiaxed crystal system with space $P\,a\,-3$. The dumb-bell shaped parasulfide ions and Fe ions appear alternately in the cubic unit cell and are arranged in a cubic centroid. The axial directions of the parasulfide ions are staggered in the structure so that the bond forces in each direction are close. The atomic radii of Fe, Co, and Ni are similar, so that their properties are very similar. The presence of Co, therefore, does not result a significant change of the pyrite crystal structure (Lin et al, 2022). However, Co could bring some imparity to the pyrite structure.

The high-spin ionic radius of bivalent hexacoordinate of Co and Fe is 0.745 and 0.780 Å, respectively (Shannon, 1976), i.e. the volume of Co-S coordination polyhedron tends to be slightly smaller than that of Fe-S coordination polyhedron. When the volume of the ligand group (Co in this case) is smaller, the space occupied by the group's electron cloud will decrease accordingly. Therefore, the Fe-S bond decreases faintly in the Co-bearing pyrite, and the octahedrons become smaller. In addition, the octahedron appears to tilt and rotate (Fig. 13, Table 2). The shrinkage of unit cell may be due to the Jahn-Teller effect, originating from the uneven distribution of electrons in the degenerate orbital of the central ion (Chandler and Bené, 1973). The incorporation of Co in the pyrite lattice structure leads to an increase of the lattice parameters (a_0).

5.3. *Insights on deposit genesis*

Zhang et al. (2002) and Feng et al. (2009, 2011) proposed a SEDEX origin for the Tuolugou deposit, indicated primarily by the occurrence of quartz albitite. Chen (2010), on the other hand, proposed a stratabound-superimposed transformation. Pan et al. (2011) suggested a SEDEX origin of the Tuolugou deposit that was subsequently affected by metamorphism.

The Co-bearing pyrite Re-Os dating indicates a mineralization age of ~ 429 Ma (Feng et al., 2009), and this is almost consistent with the zircon U-Pb age of quartz albitite of ~ 430 Ma (unpublished data) within the analytical error. This indicates that the ages of host rock and Co mineralization are at ~ 430 Ma, in Wenlock Silurian. Thus, the time of mineralization and quartz albitite is consistent within error and related to the closure of the Kunlun Ocean (Dong et al., 2018).

The eastern Kunlun orogenic belt has been evolved into composite orogenic processes that witnessed a long-lived subduction the accretionary history along southern Central Kunlun Belt (Dong et al., 2018). The SEDEX genesis ore body had experienced the Caledonian and late

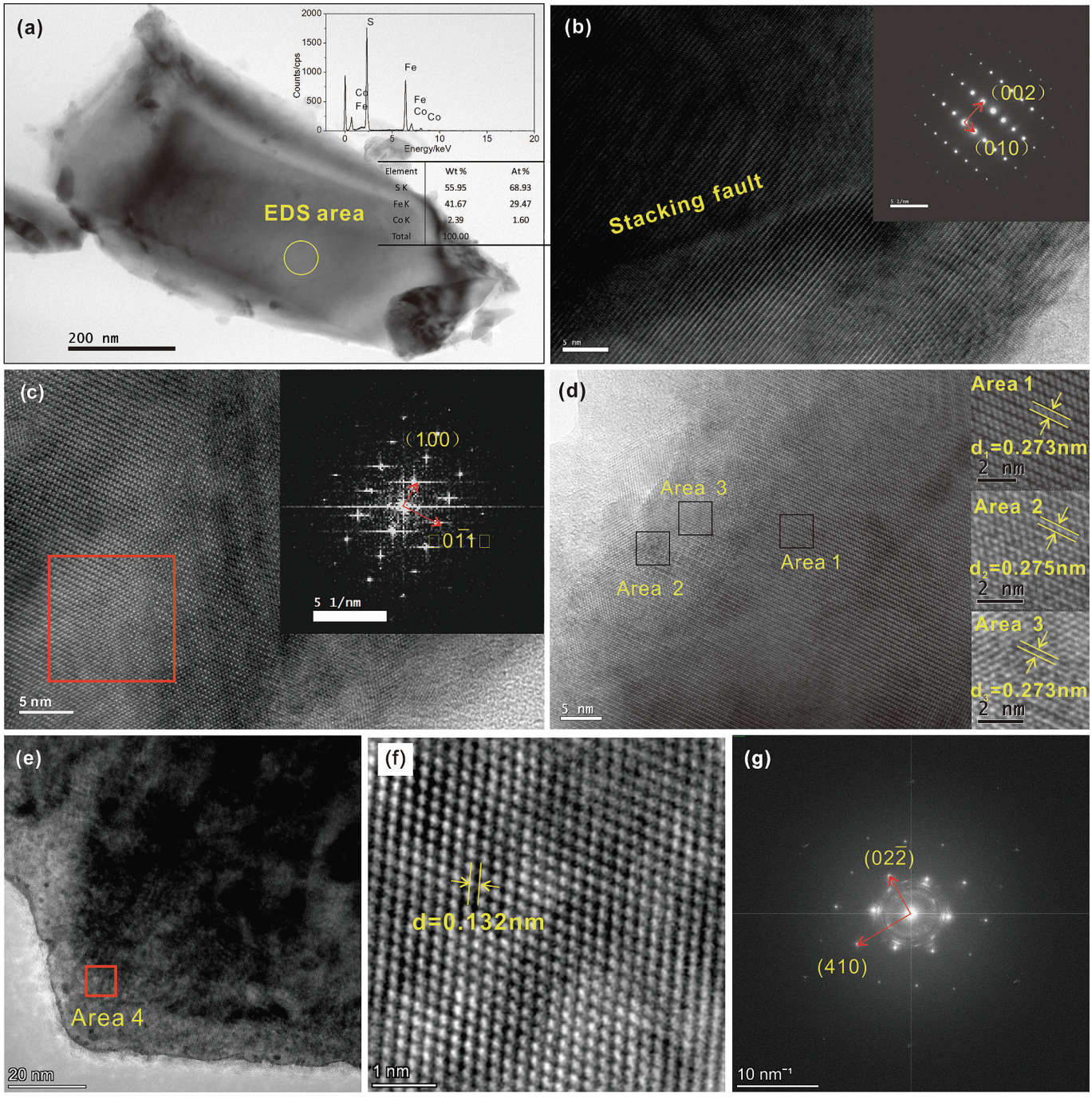

Fig. 9. TEM and HRTEM images of Py-2 sample from the Tuolugou deposit. (**a**) Morphology and EDS result. (**b**) Stacking fault and SEAD pattern. (**c**) Period-doubling. (**d**) Two-dimensional Fourier-filtered lattice image. (**e**) Pellet-shaped pyrite after a long irradiation by the HAADF-STEM electron beam. (**f**) HRTEM crystal lattice images of pyrite. (**g**) HRTEM SAED patterns of pyrite.

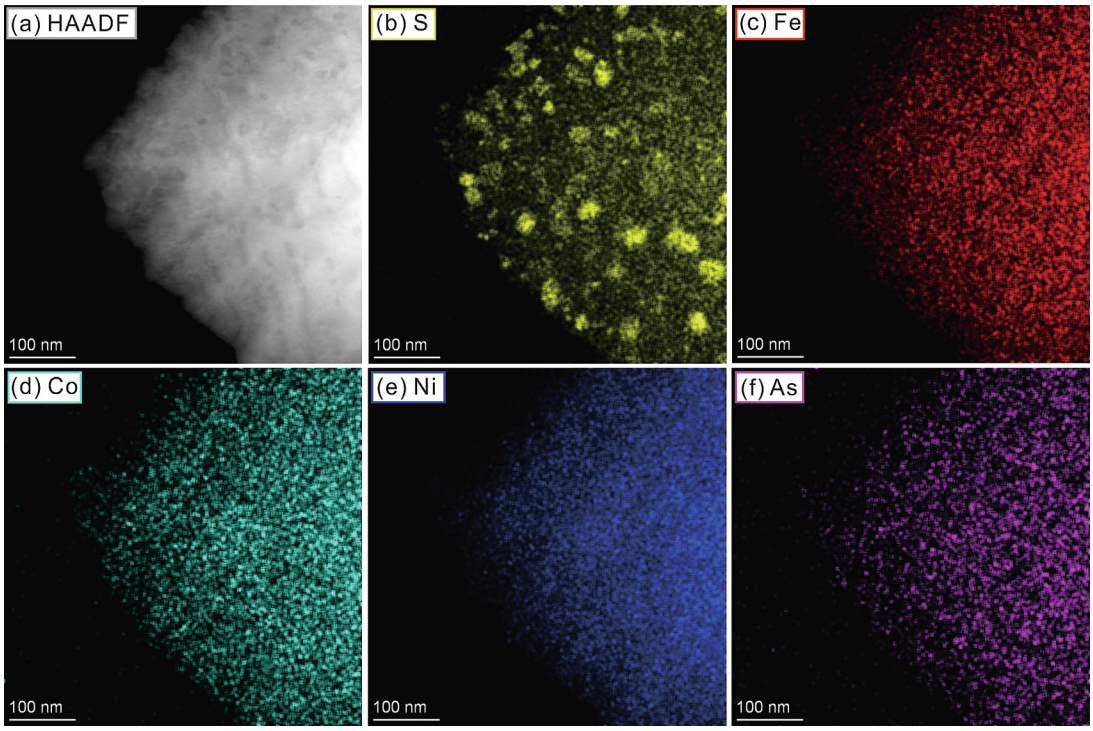

Fig. 10. (a) HAADF-STEM image and element mapping (**b-f**) of pyrite from the Tuolugou deposit.

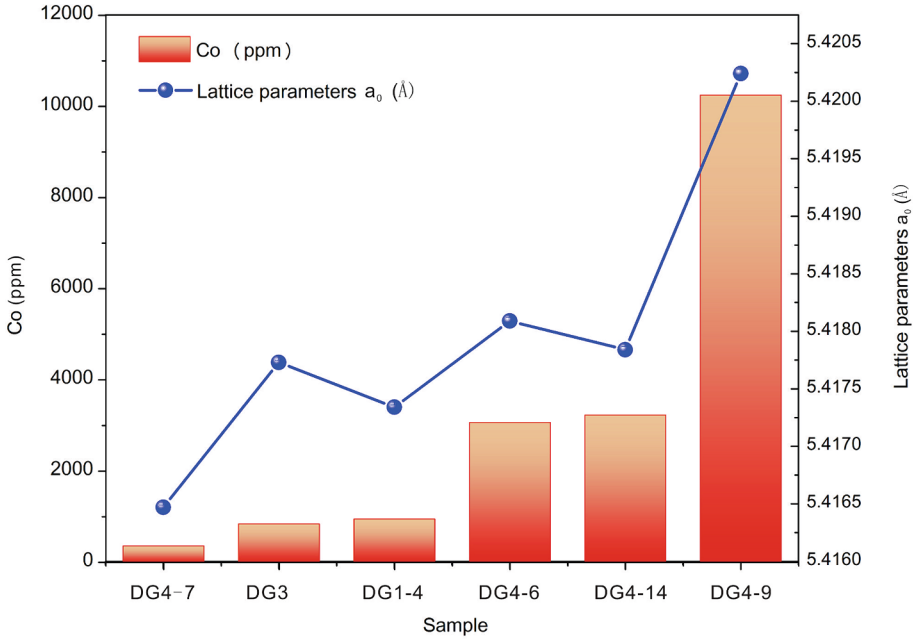

Fig. 11. Relationship between the lattice parameter (a_0) and Co content of pyrite from the Tuolugou deposit.

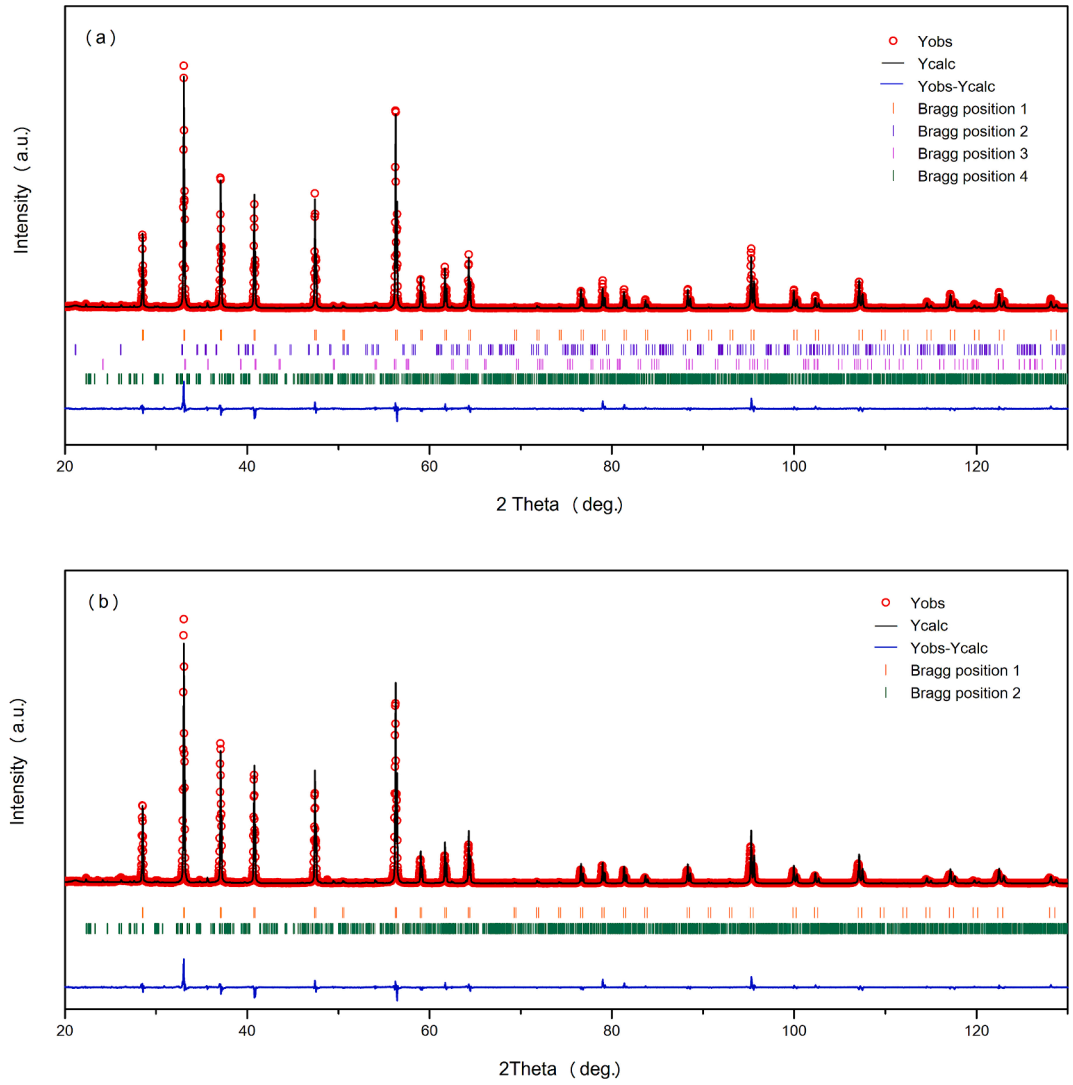

Fig. 12. Rietvield refinement of pyrite from the Tuolugou Co deposit. (**a**) Sample DG4-7, pyrite (Bragg position 1), goethite (Bragg position 2), goethite (Bragg position 3), hematite (Bragg position 4). (**b**) Sample DG4-9, pyrite (Bragg position 1), rozenite (Bragg position 2).

Table 2
Rietveld refinement of the pyrite samples from the Duangou ore section, the Tuolugou deposit.

Sample No.	S atom coordinates (Å)	Length of Fe-S bond(Å)	Length of S-S bond(Å)	Angle 1(S-Fe-S) (°)	Angle 2(S-Fe-S) (°)	Angle 3(S-Fe-S) (°)	Angle (Fe-S-Fe)(°)
DG4-7	0.38690(3)	2.26765	2.1221	37.082	94.185	85.815	115.235
DG4-9	0.38599(2)	2.26735	2.1405	37.680	94.260	85.740	115.385

Indosinian collision orogeny, leading to further enrichment of Co (Pan et al., 2011). Py-2 developed in laminated quartz albitite, which has the highest Co content (Table 1). Co content of Py-3 is lower than that of Py-2 and Co content of the fragmented fine-grained Py-3B is slightly higher than that of the coarse-grained Py-3A (Fig. 14c), which may be related to the regional metamorphic overprint. The higher Co content in pyrite reduces the Fe-S bond length and enhances the bond energy thereby increasing the hardness and brittleness of pyrite. The increase of the lattice parameters and unit cell volume also promotes congestion. These two factors can lead to the expansion of the crystal structure promoting fragmentation. This fragmentation could have resulted in fluid-induced Co enrichment during regional metamorphism.

6. Conclusion

(1) Pyrite is a significant Co-bearing ore mineral in the Tuolugou deposit. Three types of pyrite were identified. Py-2 indicates the existing of the Co-rich hydrothermal activities. Py-1 and Py-3, on the other hand, went through the neap of the SEDEX mineralization, or the very beginning (Py-1) and ending (Py-3) of the sedimentary-exhalative process.

(2) Co-Fe substitution leads to a slight increase of lattice parameters of pyrite. In the Co-bearing pyrite, the octahedrons shrink and the Fe-S bond somewhat reduces. The Jahn-Teller effect, which results from the unequal distribution of electrons in the central ion's degenerate orbital, could be the cause of the unit cell's shrinking.

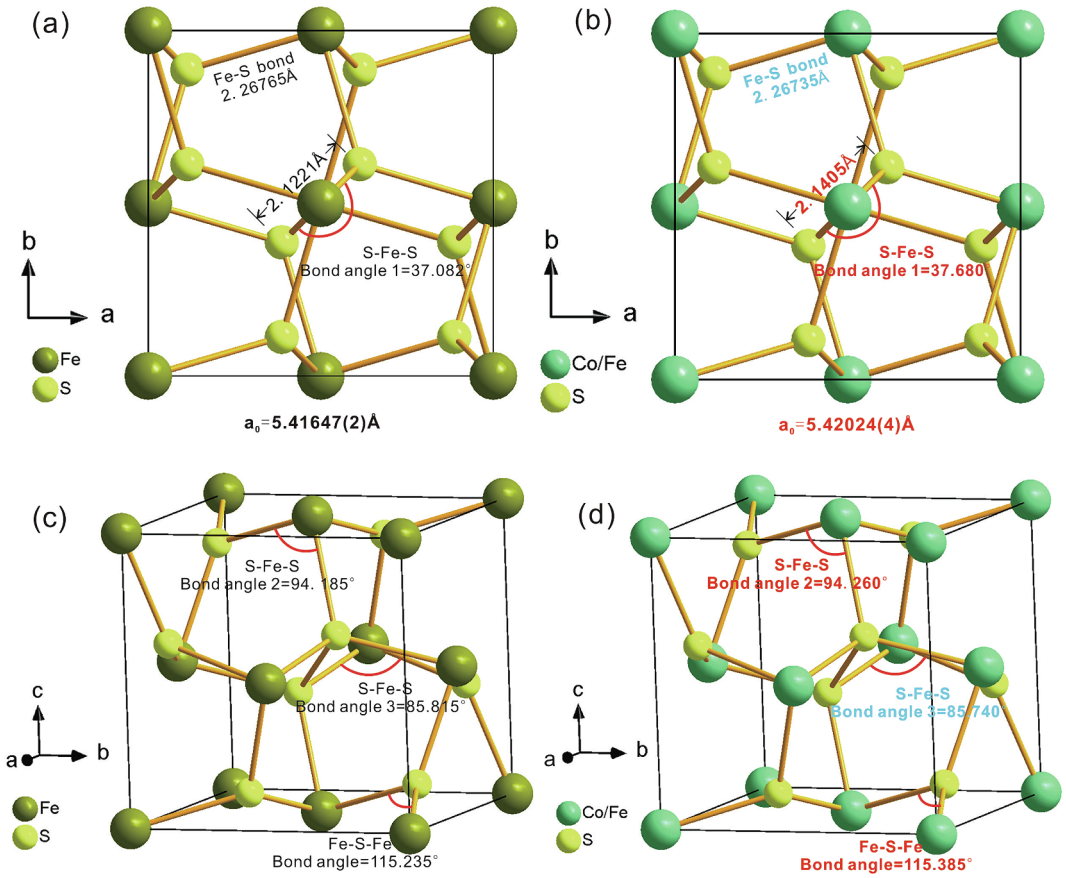

Fig. 13. Crystal structure and unit cell of (**a**, **c**) Co-barren pyrite (sample 4–7) and (**b**, **d**) Co-rich pyrite sample 4–9 (red font is the increasing parameter and blue font is the decreasing parameter).

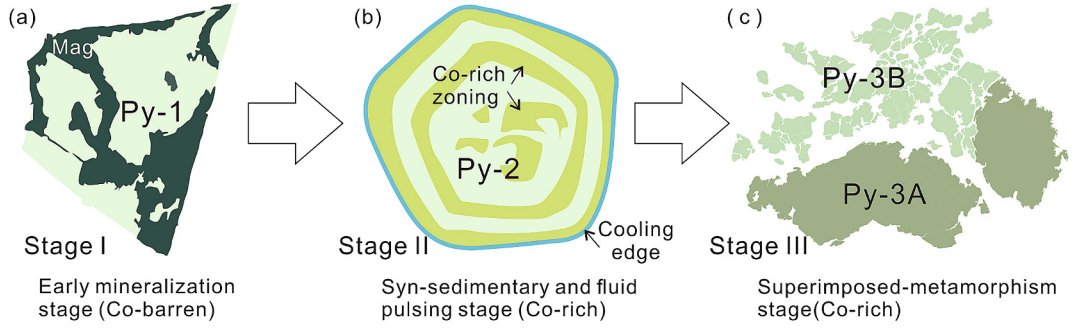

Fig. 14. Schematic diagram of the different pyrite types and mineralization stages (I-III) for the Tuolugou deposit. See text for detailed explanation.

(3) The detailed mineralogical and crystallographic study of Co-bearing pyrite are used for getting a better understanding of the Co mineralization. Co mineralization in the research area is attributed to SEDEX genesis. Subsequent metamorphism led to additional Co enrichment.

Acknowledgements and funding

This study was funded by the second comprehensive scientific investigation of the Qinghai-Tibet Plateau (grant no. 2019QZKK0801) and Science and Technology Planning Project of Guangdong Province, China (grant. No. 2020B1212060055). Bai Shenglong, Wang Jun, Zhang Jianpeng, Yu Bingfei and Pan Tong are sincerely thanked for the help during fieldwork. Gong Mingxing, Chen Tao, Wang Junping, and Chen Zhenyu are sincerely thanked for their patient help during the experiments. We thank Zhou Qifeng, Zhang Min, and Zhao Liqun for their suggestions and support.

Declaration of competing interest

The authors declare that they have no known competing financial interests or personal relationships that could have appeared to influence the work reported in this paper.

Data availability

I have shared the data in the tables and Supplementary files.

Appendix A. Supplementary data

Supplementary data to this article can be found online at https://doi.org/10.1016/j.oregeorev.2024.106176.

References

Abraitis, P.K., Pattrick, R.A.D., Vaughan, D.J., 2004. Variations in the compositional, textural and electrical properties of natural pyrite: a review. Int. J. Miner. Process. 74, 41–59.

Alam, M., Li, S.-R., Santosh, M., Shah, A., Yuan, M.-W., Khan, H., Qureshi, J.A., Zeng, Y.-J., 2019. Morphological, thermoelectrical, geochemical and isotopic anatomy of auriferous pyrite from the Bagrote valley placer deposits, North Pakistan: Implications for ore genesis and gold exploration. Ore Geol. Rev. 112, 103008.

Burn, R.G., 1993. Mineralogical Applications of Crystal Field Theory, 2nd ed. Cambridge Topics in Mineral Physics and Chemistry, Cambridge University Press, Cambridge, UK.

Chandler, R.N., Bené, R.W., 1973. EPR study of the solid solutions $Ni_xFe_{1-x}S_2$, $Co_xFe_{1-x}S_2$, and $Co_xNi_yFe_{1-x-y}S$. Phys. Rev. B 8, 4979–4988.

Chen, H.F., 2010. Discussion on the geological characteristics of Tuolugou cobalt deposit in Qinghai and the mechanism of cobalt enrichment. West China Prospect. Eng. 22, 107–110 in Chinese.

Cook, N.J., Ciobanu, C.L., Mao, J.W., 2009. Textural control on gold distribution in As-free pyrite from the Dongping, Huangtuliang and Hougou gold deposits, North China Craton (Hebei province, China). Chem. Geol. 264, 101–121.

Dong, Y., He, D., Sun, S., Liu, X., Zhou, X., Zhang, F., Yang, Z., Cheng, B., Zhao, G., Li, J., 2018. Subduction and accretionary tectonics of the East Kunlun orogen, western segment of the Central China Orogenic System. Earth Sci. Rev. 186, 231–261.

Feng, C., Qu, W., Zhang, D., Dang, X., Du, A., Li, D., She, H., 2009. Re-Os dating of pyrite from the Tuolougoustratabound Co(Au) deposit, eastern Kunlun Orogenic Belt, northwestern China. Ore Geol. Rev. 36, 213–220.

Feng, C., Qi, F., Zhang, D., Li, D., She, H., 2011. China's first independent cobalt deposit and its metallogenic mechanism: evidence from fluid inclusions and isotopic geochemistry. Acta Geol. Sin. 85, 1403–1418.

Hazen, R.M., Morrison, S.M., 2022. On the paragenetic modes of minerals: A mineral evolution perspective. Am. Mineral. 107, 1262–1287.

Hazen, R.M., Hystad, G., Golden, J.J., Hummer, D.R., Liu, C., Downs, R.T., Morrison, S. M., Ralph, J., Grew, E.S., 2017. Cobalt mineral ecology. Am. Mineral. 102, 108–116.

He, H.-L., Chen, L.-M., Song, X.-Y., Fu, B., Yi, J.-N., Yu, S.-Y., Deng, Y.-F., 2022. Genesis of the Xiarihamu magmatic Ni-Co sulfide deposit in the East Kunlun Orogen, Northern Tibetan Plateau: In situ oxygen isotope and geochemical perspectives. Econ. Geol. 117, 1827–1844.

Huang, H., Niu, Y., Zhao, Z., Hei, H., Zhu, D., 2011. On the Enigma of Nb-Ta and Zr-Hf Fractionation—A Critical Review. J. Earth Sci. 22 (1), 52–66.

Li, H.M., Shen, Y.C., Hu, Z.G., Qian, Z.Z., Liu, J.Q., Sun, J.D., 2001. Geology of Tuolugou cobalt(gold) deposit in east-Kunlun Mountains, Qinghai Province and the first discussion on its genesis. Geol. Prospect. 37, 60–64.

Li, W., Wang, J., Cui, M., Liu, X., Jia, L., Chen, K., Wu, S., Gao, B., Xue, D., Liu, Y., Li, C., Luo, Y., Su, B., 2023. Natural clinopyroxene reference materials for in situ microanalysis. Geostand. Geoanal. Res. 47 (1), 199–210.

Lin, X., Xia, Y., Wei, G., Zhou, J., Liang, X., Xian, H., Zhu, J., He, H., 2022. Distinct effects of transition metal (cobalt, manganese and nickel) ion substitutions on the abiotic oxidation of pyrite: In view of hydroxyl radical production. Geochim. Cosmochim. Acta 321, 170–183.

Lu, A.H., 2022. Mineral evolution heralds a new era for mineralogy. Am. Mineral. 107, 1217–1218.

Lu, Y.-T., Chien, Y.-J., Liu, C.-F., You, T.-H., Hu, C.-C., 2017. Active site-engineered bifunctional electrocatalysts of ternary spinel oxides, $M_{0.1}Ni_{0.9}Co_2O_4$ (M: Mn, Fe, Cu, Zn) for the air electrode of rechargeable zinc–air batteries. J. Mater. Chem. A 5, 21016–21026.

Ma, G., Beaudoin, G., Qi, S., Ying, L., 2004. Geology and geochemistry of the Changba sedex Pb-Zn deposit, Qinling orogenic belt. China. Mineralium Deposita 39 (3), 380–395.

Niu, Y., 2012. Earth processes cause Zr-Hf and Nb-Ta fractionations, but why and how? RSC Adv. 2, 3587–3591.

Niu, S.-D., Li, S.-R., Santosh, M., Zhang, D.-H., Li, Z.-D., Shan, M.-J., Lan, Y.-X., Gao, D.-R., Zhao, W.-B., 2016. Mineralogical and isotopic studies of base metal sulfides from the Jiawula Ag–Pb–Zn deposit, Inner Mongolia, NE China. J. Asian Earth Sci. 115, 480–491.

Niu, S.D., Wu, H.Y., Zhang, J.P., Niu, X.L., Wang, Y.C., Lin, X.J., Santosh, M., Chen, J.H., 2023. Supergene Hydrous Sulfates in the Tuolugou Co-Au Deposit, Northern Qinghai-Tibet Plateau: Implications for Genetic Mechanism and Exploration. Minerals 13, 1198. https://doi.org/10.3390/min13091198.

Pan, T., By, Y.S., Sun, F.Y., Chen, J.P., 2011. Mineralization series and mineralization prediction of nonferrous and noble metals in East Kunlun Qinghai Province. Geological Press, Beijing, pp. 105–119 in Chinese.

Qiu, Z.-J., Fan, H.R., Goldfarb, R., Tomkins, A.G., Yang, K.F., Li, X., Xie, L., Liu, X., 2021. Cobalt concentration in a sulfidic sea and mobilization during orogenesis: Implications for targeting epigenetic sediment-hosted Cu-Co deposits. Geochim. Cosmochim. Acta 304, 1–18.

Rietveld, H.M., 1967. Line profiles of neutron powder-diffraction peaks for structure refinement. Acta Crystallogr. 22, 151–152.

Rodríguez-Carvajal, J., 1993. Recent advances in magnetic structure determination by neutron powder diffraction. Phys. B Condens. Matter 192, 55–69.

Shannon, R.D., 1976. Revised effective ionic radii and systematic studies of interatomic distances in halides and chalcogenides. Acta Crystallogr. Sect. A: Cryst. Phys., Diffr., Theor. Gen. Crystallogr. 32, 751–767.

Slack, J.F., Kimball, B.E., Shedd, K.B., 2017. Cobalt, Chapter F, in Schulz, K.J., DeYoung, J.J.H., Seal Ii, R.R., Bradley, D.C., eds., Critical mineral resources of the United States—Economic and environmental geology and prospects for future supply. U.S. Geological Survey, Professional Paper 1802, F1-F40.

Song, S.G., Bi, H.Z., Qi, S.S., Yang, L.M., Allen, M.B., Niu, Y.L., Su, L., Li, W.F., 2018. HP–UHP Metamorphic belt in the East Kunlun orogen: Final closure of the Proto-Tethys ocean and formation of the Pan-North-China Continent. J. Petrol. 59, 2043–2060.

Su, B., Qin, K., Jiang, S., Cao, M., Zhang, Z., Zhang, H., Xue, G., Zhou, T., Mo, J., 2023. Mineralization regularity, scientific issues, prospecting technology and research prospect of Co-Ni deposits in China. Acta Petrol. Sin. 39 (4), 968–980 in Chinese with English abstract.

Su, W., Schwarzenbach, E.M., Chen, L., Li, Y., John, T., Gao, J., Chen, F., Hu, X., 2019. Sulfur isotope compositions of pyrite from high-pressure metamorphic rocks and related veins (SW Tianshan, China): Implications for the sulfur cycle in subduction zones. Lithos 348–349, 105212.

Sun, S.S., McDonough, W.F. 1989. Chemical and isotopic systematics of oceanic basalts: Implications for mantle composition and processes. In: Saunders, A.D., Norry, M.J. (Eds.), Magmatism in Ocean Basins. Geological Society of London, Special Publication 42, 313-345.

Sun, X., Li, R.Y., Sun, H.Y., Olin, P.H., Santosh, M., Fu, B., Deng, J., 2024. Genesis of Pb–Zn-Ag-Sb mineralization in the Tethys Himalaya, China: Early magmatic-hydrothermal Pb–Zn(-Ag) mineralization overprinted by Sb-rich fluids. Miner. Deposita. https://doi.org/10.1007/s00126-024-01264-5.

Vasyukova, O.V., Williams-Jones, A.E., 2022. Constraints on the genesis of cobalt deposits: Part II Applications to Natural Systems. Econ. Geol. 117, 529–544.

Wang, P., Zhao, G.C., Liu, Q., Yao, J.L., Han, Y.G., 2022. Evolution of the Paleo-Tethys Ocean in Eastern Kunlun, North Tibetan Plateau: From continental rift-drift to final closure. Lithos 422–423, 1–15.

Witt, W.K., Hagemann, S.G., Roberts, M., Davies, A., 2020. Cobalt enrichment at the Juomasuo and Hangaslampi polymetallic deposits, Kuusamo Schist Belt, Finland: a role for an orogenic gold fluid? Miner. Deposita 55, 381–388.

Wu, S., Wörner, G., Jochum, K.P., Stoll, B., Simon, K., Kronz, A., 2019. The preparation and preliminary characterisation of three synthetic andesite reference glass materials (ARM-1, ARM-2, ARM-3) for in situ microanalysis. Geostand. Geoanal. Res. 43, 567–584.

Xian, H.Y., Du, R.X., Zhu, J.X., Chen, M., Tan, W., Zhu, R.L., Wei, J.M., He, H.P., 2018. Hydration induced bandgap shift at pyrite-water interface. Appl. Phys. Lett. 113, 123901.

Xian, H.Y., Zhu, J.X., Tan, W., Tang, H.M., Liu, P., Zhu, R.L., Liang, X.L., Wei, J.M., He, H.P., Teng, H.H., 2019. The mechanism of defect induced hydroxylation on pyrite surfaces and implications for hydroxyl radical generation in prebiotic chemistry. Geochim. Cosmochim. Acta 244, 163–172.

Xu, Z., Yang, J., Jiang, M., Li, H., Xue, G., Yuan, X., Qian, H., 2001. Deep structure and lithospheric shear faults in the East Kunlun-Qiangtang region, northern Tibetan Plateau. Sci. China Ser. D Earth Sci. 44, 1–9.

Xue, D., Li, W., Wang, J., Jia, L., Mao, Y., Su, B., 2023. Advances in analysis for cobalt and nickel in geological materials. Acta Petrol. Sin. 39 (4), 1217–1232 in Chinese with English abstract.

Yang, S.Y., Jiang, S.Y., Mao, Q., Chen, Z.Y., Rao, C., Li, X.L., Li, W.C., Yang, W.Q., He, P. L., Li, X., 2022. Electron probe microanalysis in geosciences: Analytical procedures and recent advances. At. Spectrosc. 43, 186–200.

Yu, M., Dick, J.M., Feng, C.Y., Li, B., Wang, H., 2020. The tectonic evolution of the East Kunlun Orogen, northern Tibetan Plateau: A critical review with an integrated geodynamic model. J. Asian Earth Sci. 191, 1–23.

Yuan, M.-W., Li, S.-R., Li, C.-L., Santosh, M., Alam, M., Zeng, Y.J., 2018. Geochemical and isotopic composition of auriferous pyrite from the Yongxin gold deposit, Central Asian Orogenic Belt: Implication for ore genesis. Ore Geol. Rev. 93, 255–267.

Zhang, H., Cai, Y., Sha, G., Brugger, J., Pring, A., Ni, P., Qian, G., Luo, Z., Zhang, Y., Tan, W., 2021. Effects of arsenic on the distribution and mode of occurrence of gold during fluid-pyrite interaction: A case study of pyrite from the Qiucun gold deposit, China. Am. Mineral. 107, 914–929.

Zhang, H., Qian, G., Cai, Y., Gibson, C.T., Pring, A., 2022. Crystal chemistry of arsenian pyrites: A Raman spectroscopic study. Am. Mineral. 107, 274–281.

Zhu, J.X., Xian, H.Y., Lin, X.J., Tang, H.M., Du, R.X., Yang, Y.P., Zhu, R.L., Liang, X.L., Wei, J.M., Teng, H.H., He, H.P., 2018. Surface structure-dependent pyrite oxidation in relatively dry and moist air: Implications for the reaction mechanism and sulfur evolution. Geochim. Cosmochim. Acta 228, 259–274.